Coregistered three-dimensional ultrasound and photoacoustic imaging system for ovarian tissue characterization

Andres Aguirre
Puyun Guo
John Gamelin
Shikui Yan
University of Connecticut
Department of Electrical and Computer Engineering
371 Fairfield Way
Storrs, Connecticut 06269

Mary M. Sanders
University of Connecticut Health Center
Department of Pathology
263 Farmington Avenue
Farmington, Connecticut 06030

Molly Brewer
University of Connecticut Health Center
The Carole and Ray Neag Comperhensive Cancer Center
263 Farmington Avenue
Farmington, connecticut 06030

Quing Zhu
University of Connecticut
Department of Electrical and Computer Engineering
371 Fairfield Way; U-2157
Storrs, Connecticut 06269
E-mail: zhu@engr.uconn.edu

Abstract. Ovarian cancer has the highest mortality of all gynecologic cancers, with a five-year survival rate of only 30% or less. Current imaging techniques are limited in sensitivity and specificity in detecting early stage ovarian cancer prior to its widespread metastasis. New imaging techniques that can provide functional and molecular contrasts are needed to reduce the high mortality of this disease. One such promising technique is photoacoustic imaging. We develop a 1280-element coregistered 3-D ultrasound and photoacoustic imaging system based on a 1.75-D acoustic array. Volumetric images over a scan range of 80 deg in azimuth and 20 deg in elevation can be achieved in minutes. The system has been used to image normal porcine ovarian tissue. This is an important step toward better understanding of ovarian cancer optical properties obtained with photoacoustic techniques. To the best of our knowledge, such data are not available in the literature. We present characterization measurements of the system and compare coregistered ultrasound and photoacoustic images of ovarian tissue to histological images. The results show excellent coregistration of ultrasound and photoacoustic images. Strong optical absorption from vasculature, especially highly vascularized corpora lutea and low absorption from follicles, is demonstrated. © 2009 Society of Photo-Optical Instrumentation Engineers. [DOI: 10.1117/1.3233916]

1 Introduction

Photoacoustic imaging has emerged as a promising biomedical imaging technique, in which a short-pulsed laser beam penetrates into the tissue sample diffusively.[1–15] The photoacoustic waves, due to thermoelastic expansion resulting from a transient temperature rise caused by the laser irradiation, are then measured around the sample by wideband ultrasound transducers. The acquired photoacoustic waves are used to reconstruct, at ultrasound resolution, the optical absorption distribution that reveals optical contrast, which is directly related to neovascularization associated with tumor angiogenesis[16] in the near-infrared (NIR) spectrum. As reported in Ref. 6, optical absorption of hemoglobin is roughly ten times higher than that of the surrounding tissue at 850 nm, and about 100 times at 550 nm. Angiogenesis is a key process for tumor growth and metastasis.[17,18] Photoacoustic techniques combine the high-contrast advantage of optical imaging with the high-resolution advantage of ultrasound imaging. Provided that enough light fluence is delivered, the penetration depth is scalable with ultrasound frequency. In the diagnostic frequency range of 3 to 8 MHz, the penetration depth in tissue can reach 2 to 3 cm using NIR light.[19]

Several research groups have explored photoacoustic systems for a variety of applications that can be categorized as tomography systems[2,4,19–22] and linear array systems.[23–27] For tomographic systems, either a single ultrasound transducer or an array transducer is used to acquire photoacoustic waves around a sample. Imaging is performed using tomographic algorithms, such as back-projection. For linear array systems, an ultrasound array is used to acquire photoacoustic waves from a limited angle around the sample. Images are reconstructed using a variety of methods such as back-projection, Fourier, or delay-and-sum algorithms.[28–30] The imaging quality is, in general, poorer than that of tomographic systems due to a limited field of view. However, the advantages of using a linear array system are that: 1. it can be adapted from a standard pulse-echo commercial ultrasound system to provide coregistered dual-modality ultrasound and photoacoustic imaging, and 2. it provides greater flexibility to image tissue with limited accessibility.

Address all correspondence to: Quing Zhu, Department of Electrical and Computer Engineering, University of Connecticut, 371 Fairfield Way; U-2157, Storrs, CT 06269. Tel: 860-486-5523; Fax: 860-486-2447; E-mail: zhu@engr.uconn.edu860

Ideally, for 3-D volumetric imaging, 2-D arrays are desirable because they can acquire the entire 3-D information without mechanical scanning. Additionally, they can provide the same resolution and field of view size in elevation as they do in azimuth.[31] However, the number of elements increases rapidly as N^2, where N is the number of elements in either dimension. As an example, if $N=64$, a total of 4096 elements would be needed for the 2-D array. This large number of elements presents considerable technical challenges: fabrication, cross talk, interconnection, signal-to-noise ratio, complexity of electronics, etc. To balance the 3-D imaging need and the system complexity, 1.75-dimensional (1.75-D) arrays have been developed.[32,33] These arrays have similar element size in azimuth compared with 2-D arrays, while in elevation the element size is considerably larger, thus limiting beam steering in elevation to a certain degree

We have developed an ultrasound system based on a 1.75-D transducer array. Coregistered 3-D ultrasound and photoacoustic imaging can be readily obtained, which allows us to visualize tissue structures and functional information simultaneously over a large field of view. The system has been used to acquire volumetric coregistered ultrasound and photoacoustic images of ovarian tissue. The photoacoustic images, to the best of our knowledge, provide for the first time characterization of normal ovarian tissue that reveals its optical properties using a photoacoustic technique. Such information is indispensable for future studies aiming to diagnose ovarian diseases (e.g., ovarian cancer) using photoacoustic techniques.

Ovarian cancer has the highest mortality of all gynecologic cancers.[34] 70% percent of women with ovarian cancer will die within 5 to 7 years of diagnosis.[35] Cancers with high mortalities, such as ovarian cancer, warrant effective methods of early detection. The current imaging technologies are not capable of detecting early cancers due to poor sensitivity and specificity.[36–38] Thus, many women are not correctly diagnosed until the cancer becomes widely metastatic, which is associated with poor survival. On the other hand, the majority of women who possess a detectable ultrasound abnormality do not harbor a cancer. They all will undergo unnecessary oophorectomy (with only a 1 to 3% risk of having a cancer), or they will be followed conservatively and may have a cancer that is not detected until metastasis develops. New imaging techniques, such as photoacoustic imaging, that can provide functional and molecular contrasts could improve the specificity of ultrasound for ovarian cancer detection and characterization.

The long-term goal is to develop coregistered transvaginal probes for noninvasive evaluation of early angiogenic changes in the ovary. The ability to target early angiogenic changes in the ovary with an imaging modality would greatly enhance the care for women at risk for ovarian cancer. In this work, we first describe our coregistered 3-D ultrasound and photoacoustic imaging system and present characterization measurements. Next, we present coregistered images of porcine ovaries and compare them to histological images. At the end, we discuss design considerations for the development of next-generation photoacoustic imaging systems for noninvasive ovarian cancer detection.
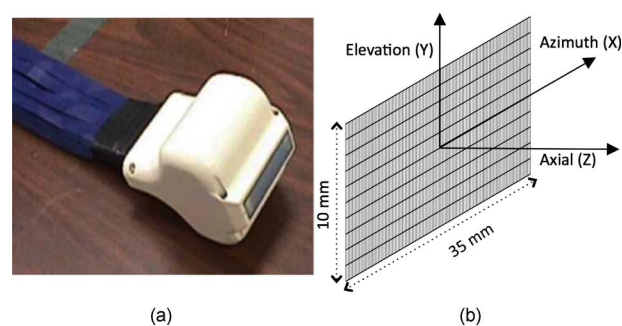
Fig. 1 The 1.75-D ultrasound transducer array. (a) Actual picture with coaxial cable interconnection. (b) Scanning geometry diagram.

2 Materials and Methods

2.1 System Description

Our ultrasound imaging system is composed of a 1.75-D ultrasound phase array purchased from Tetrad Corporation (now W. L. Gore and Associates, Incorporated, Newark, Delaware) and electronic circuitry developed in our laboratory. The array has ten rows in elevation and 128 elements in each row, totaling 1280 elements (see Fig. 1). We have previously demonstrated that it is capable of electronically scanning a volume of 80 and 20 deg in the azimuth and elevation directions, respectively.[39,40] The transducer operates at a central frequency of 5 MHz with 60% bandwidth. The element height in the elevation direction is 0.97 mm, and the element width in azimuth is 0.224 mm.[41] An acoustic lens focuses the beam in elevation 40 mm away from the transducer. The 1280-pin outputs are bundled in 40 groups of cables, each containing 32 thin 50-ohm coax cables of 1.75 m in length.

The circuitry consists of four identical 320-channel transmit (TX) and receive multiplexer (MUX) unit pairs (Fig. 2). Each TX board provides dedicated transmission drivers for 320 channels with transmit/receive isolation. The TX unit can drive each array element independently and simultaneously, with an adjustable time delay and pulse width resolution of 20 ns. The paired MUX units multiplex the 320 channels into ten parallel outputs that are independently amplified by two-stage variable gain (nominal = 60 dB) amplifiers and filtered with 1- to 10-MHz bandpass filters. A common data acquisition unit multiplexes the $4 \times 10 = 40$ channels from the for TX/MUX pairs for digitization by a 12-bit, 50-MS/s analog-to-digital converter. All modules are controlled with custom C-language software in the host PC through two National Instruments (Austin, Texas) PCI-DIO-32HS high-speed digital I/O cards.

The system can operate under two modes: conventional ultrasound pulse-echo mode and photoacoustic mode. Both the 3-D ultrasound images and photoacoustic images are reconstructed using a typical delay and sum algorithm based on the transducer array geometry. The algorithm has been implemented in C-language.

In conventional pulse-echo ultrasound imaging mode, users can select a fixed transmission focal depth, number of scan angles, and total range in azimuth and elevation. The transmission circuitry generates high voltage pulses that activate the 1.75-D ultrasound array, and the desired acoustic beams are transmitted into the tissue. The return signals from the
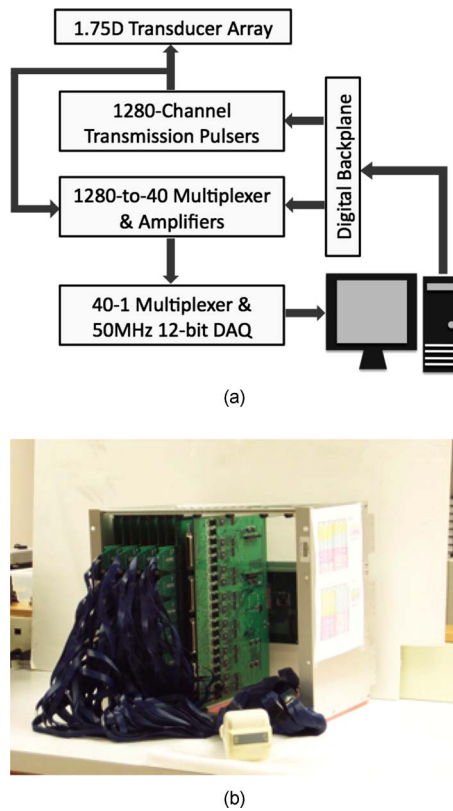
Fig. 2 3-D ultrasound and photoacoustic imaging system. (a) Schematic diagram of the system. (b) Actual photograph of the system with the array.

array are multiplexed, amplified, and sampled by the data acquisition unit. For each angular location, this transmission sequence is repeated to retrieve the data for all elements. After the data acquisition is finished, the acquired rf data is loaded into the computer memory for filtering, beam forming, and imaging. The rf data from all 1280 channels is used to form the beams. It takes approximately seven seconds to acquire the data and generate the beam for each angular direction. Dynamic focusing in reception has been implemented in software with focusing at every four samples.

In photoacoustic imaging mode, the transmission (TX) circuitry is disabled and only the MUX unit and DAQ unit are enabled. A Ti:Sapphire (Symphotics TII, LS-2134, Symphotics, Camarillo, California) optically pumped with a Q-switched Nd:YAG laser (Symphotics-TII, LS-2122), illuminates the sample orthogonal to the azimuth-axial imaging plane of the transducer. The laser delivers 8- to 12-ns pulses at 15 Hz with tunable wavelengths from 700 to 950 nm. The beam is diverged with a planoconcave lens and homogenized by a circular profile engineered diffuser (ED1-S20, ThorLabs, Newton, New Jersey) to produce uniform illumination on the sample. A scan starts by triggering the circuitry from the laser at the instant when the optical pulse illuminates the tissue. The received electrical signals are amplified, filtered, and digitized. Raw data are transferred into the host PC for further beam forming. It takes approximately one and a half minutes to retrieve the 1280-channel data under this mode. Then, similar to the pulse-echo mode, the acquired rf data is loaded into

the computer memory for filtering, beam forming, and imaging. Delay and sum with dynamic focusing at every four samples is used to form the photoacoustic image.

2.2 System Characterization

In pulse-echo mode, we measured the two-way transmission reception and the one-way transmission-only beam profiles using a 1.0-mm diameter polyvinylidine fluoride (PVDF) hydrophone. By acoustic reciprocity, the one-way transmission beam profile is equivalent to the one-way photoacoustic reception beam profile. The hydrophone, which was used both as a receiver and a target, is broadband with a flat frequency response between 1 and 10 MHz and a sensitivity of 0.1 µV/Pa (Force Institute, Copenhagen). It was connected to an ultrasound pulser-receiver (Panametrics 5072PR) to measure the ultrasound signals transmitted by the 1.75-D array. Both the hydrophone and the 1.75-D transducer array were submerged in castor oil, which has an acoustic absorption of 11.9 dB/cm at 5 MHz and 20 °C,[42] close to that of soft tissue. The hydrophone, facing the 1.75-D array, was fixed at zero degrees in the azimuth and elevation directions with respect to the center of the array, and 40 mm depth in the axial direction. Sector scans of 40 and 20 deg were performed on the azimuth-axial and elevation-axial imaging planes respectively, while the transmission focus of the system was kept at 40 mm [Fig. 3(a)]. For each individual angular scan, the transmitted signals were measured by the hydrophone, while the 1.75-D transducer measured the reflected signals from the hydrophone. The one-way beam profile of the system was obtained by measuring the peak value of the received signal envelope from the hydrophone at each angular position. The two-way beam profile was acquired by measuring the peak value of the envelope of the beam-formed transducer signal at each angular scan.

The field of view of the 1.75-D array was evaluated by measuring the two-way beam profiles in azimuth and elevation at different points across the field using a similar setup as discussed before. In this case, a rigid music string with a diameter of 0.5 mm was used as the point-like target instead of the hydrophone. The measurements were grouped in three sets. For the first set, the target was kept at zero degrees in the azimuth and elevation directions of the array, while the separation distance (axial) between the target and the array was varied to 20, 40, and 50 mm. At each axial position, measurements were acquired by focusing the ultrasound array to the location of the target. For the second set of measurements, the target was kept at zero degrees in the elevation plane and it was translated in the azimuth-axial plane while keeping its distance from the center of the array at 40 mm. The angular locations at which the measurements were taken for this set were 0, 20, and 39 deg. The transmission focus was kept at 40 mm for these three locations. For the last set, the target was fixed at zero degrees in the azimuth plane, while it was translated in the elevation-axial plane in an arc. The target locations, at which measurements were taken with a transmission focus fixed at 40 mm, were 0, 5, and 10 deg. For all three sets of measurements, the two-way beam profiles in azimuth and elevation were obtained by performing sector scans and measuring the peak values of the envelope of the formed beams at the corresponding depth of the target.

(a)

(b)
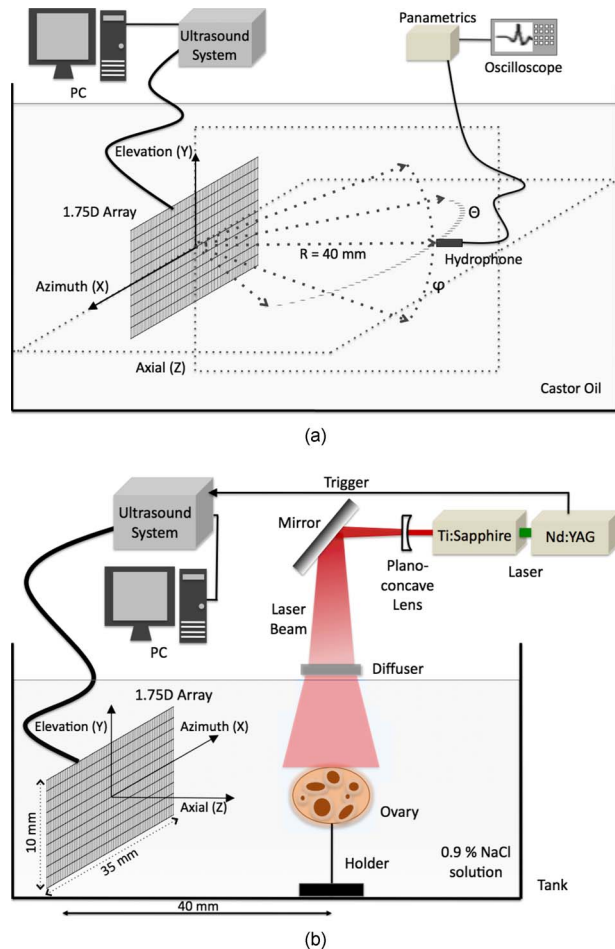
Fig. 3 System characterization and ovary imaging setups. (a) Experimental setup for one-way versus two-way measurements using a hydrophone as an active target. A similar setup was used for measurements across the field of view, where the hydrophone was replaced by a music string that was positioned at different locations. (b) Experimental setup for ultrasound and photoacoustic imaging of ovaries.

Resolution measurements for pulse-echo ultrasound and photoacoustic modes were performed using a black nylon thread with 80 μm in diameter. To measure the azimuth resolution, the thread was suspended perpendicular to the azimuth-axial imaging plane at a slight angle ($<$20 deg) to the incident laser beam. For the elevation resolution measurement, the thread was placed parallel to the azimuth-axial imaging plane and to the array front face. With the transducer and the thread submerged in water with a separation of 40 mm, sector scans were performed in the azimuth and in elevation. The measured -6-dB full-width half-maximum (FWHM) from the beam profiles of the thread was used to obtain the resolutions. Subtraction of the 80-μm thread diameter from the FWHM yields corrected resolution measurements both in azimuth and elevation. The results were compared to theoretical values. Since there is no theory for wideband transducer arrays, the narrowband theory is commonly used to estimate their performance.[43] For pulse-echo mode, the narrowband theory indicates that the beam profile follows a $\mathrm{sinc}^2(L_x x/\lambda z)$ pattern in the azimuth direction, where L_x is the transducer size in the azimuth direction x, λ is

the wavelength, and z is the depth. One can estimate the azimuth resolution as the value of x when the sinc^2 function reduces to 0.5. In the elevation direction, the beam profile follows a $\mathrm{sinc}^2(L_y y/\lambda z)$ pattern, where L_y is the dimension of the transducer in the elevation direction y. Following the same procedure described for estimating the azimuth resolution, the elevation resolution can be obtained. In photoacoustic mode, the beam profiles follow similar patterns, with the exception that they are given by a sinc function pattern instead of a sinc^2 function.

2.3 Simulations

Further verification of our imaging system was achieved by comparing the system's measured response to simulations. The simulations were performed using Field II simulation software[44,45] and Matlab®. Field II can simulate pulsed and continuous wave pressure fields generated from ultrasound transducers and arrays of arbitrary shape, apodization, or excitation function. It comprises a set of libraries that can be called from within the Matlab® programming environment. The libraries model the behavior of ultrasound transducers of arbitrary geometry, including an elevation focused linear multirow transducer that was used in this study.

2.4 Ovary Imaging

Porcine ovaries freshly excised from local farms were studied with our imaging system. Ovaries were kept in a 0.9% w/v NaCl solution from the time they were removed from the animal and during the imaging process. Sector scans in the azimuth direction were performed both in pulse-echo ultrasound and photoacoustic mode at different elevations without mechanically moving the sample or the transducer. The sample was placed close to the 40-mm elevation focus of the transducer in the axial direction and centered in the azimuth direction [Fig. 3(b)]. In photoacoustic mode, the wavelength of the laser was adjusted to 740 nm and the incident power was maintained below 8 mJ/cm². The obtained ultrasound and photoacoustic images were superimposed to provide structural guidance for interpretation of the photoacoustic results.

After imaging experiments, the ovaries were submerged in 37% formalin at room temperature for 24 h. After fixation, they were rinsed with fresh water, placed in a 0.9% w/v NaCl solution, and kept at 4 °C. For histological evaluation, the ovaries were cut in 5-mm blocks parallel to the imaging plane, dehydrated with graded alcohol, embedded in paraffin, and sectioned to 7-μm thickness using a paraffin microtone. Slides corresponding to the imaged planes were stained using hematoxylin and eosin (HE).

3 Results

3.1 System Characterization

The measured one-way and two-way beam profiles using a hydrophone, both in azimuth and elevation, agree with simulation results as shown in Figs. 4(a), 4(b), 5(a), and 5(b), respectively. In transmission or reception mode, the one-way radiation pattern of an ultrasound array at the focal zone is the Fourier transform of the array's excitation aperture. In pulse-echo mode, the effective aperture is the autocorrelation of the
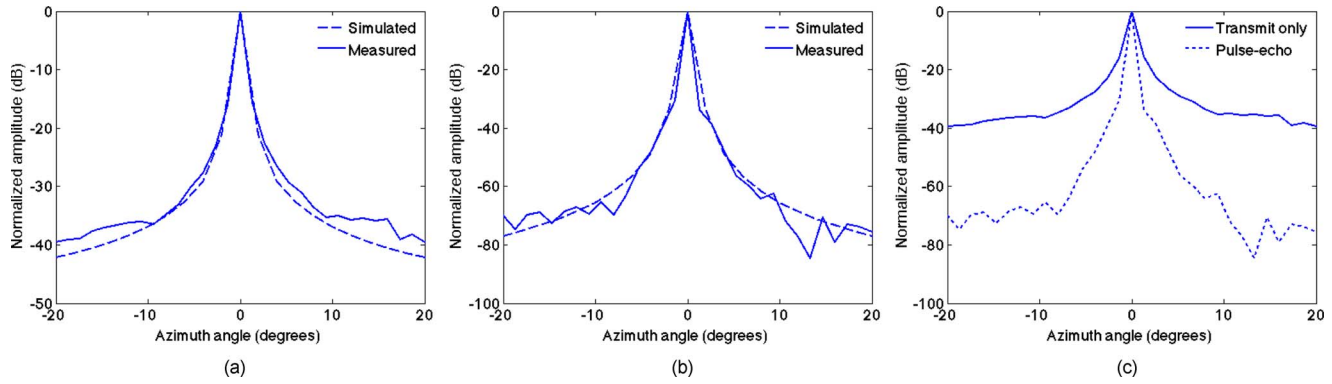
Fig. 4 Measured and simulated azimuth beam profiles of a 40-deg sector scan: (a) transmit only, (b) pulse-echo, and (c) transmit only versus pulse-echo.

array's aperture pattern.[46] Hence, the two-way beam profile is equivalent to squaring the one-way profile. In Figs. 4(c) and 5(c), the measured one-way and two-way azimuth and elevation beam profiles are shown. Because of the logarithmic scale used, a two-fold difference between the one-way and two-way profiles is obtained as predicted by theory.

From the first group of measurements across the field of view, where the sample was moved axially, it can be observed [Figs. 6(a) and 6(b)] that the beam profile, both in azimuth and elevation directions, remain fairly constant at 40 and 50 mm away from the transducer on the central axis. At 20 mm, the measured beam profiles get wider, which translates into lower angular resolution at this point. This widening is due to the limited individual element directivity, which has a FWHM at -6 dB of 76 deg in azimuth and 18 deg in elevation. Directivity imposes a limit on the number of elements that effectively receive signal from a given point in the field of view of the array. When imaging a point target on the central axis, theory suggests that for our 1.75-D transducer array, the array effective aperture reduces for points within 30 mm from the transducer array, reducing the resolution at these points.

Similarly, for the second group of measurements across the field of view, the results show [Figs. 6(c) and 6(d)] expected variations in the width of the azimuth and elevation beam profiles due to directivity and steering effects. At 40 deg in the azimuth, the beam profiles are the broadest of all at the three measured locations. At this point the width of the elevation

beam profile has almost doubled compared to the no-steering beam profile. On the other hand, for the third group of measurements moving the target in elevation, no significant change of the beam widths is observed due to the small focusing deflections (up to 10 deg) used.

The measured resolution in pulse-echo mode, both in azimuth and elevation, agree very well with theoretical values. From the narrowband theory, the FWHM of the main lobe for the 1.75-D transducer is estimated to be 0.45 deg in azimuth and 1.55 deg in elevation 40 mm away from the transducer. The measured resolutions, after subtracting the diameter of the target thread, are 0.51 deg in azimuth and 1.52 deg in elevation for the pulse-echo mode. Similarly, for photoacoustic mode, the narrowband theory suggests the resolution is 0.60 deg in azimuth and 2.13 deg in elevation. The measured resolutions in photoacoustic mode are 0.76 deg in azimuth and 2.55 deg in elevation, after subtracting the diameter of the target. A plot comparing the resolution measurement results in pulse-echo and photoacoustic modes is shown in Fig. 7.

3.2 Ovary Imaging

Coregistered images of the ovaries show excellent correlation of the ultrasound and photoacoustic features when compared to histological images. In all three cases, ultrasound reveals the presence of antral follicles. The ovarian follicle consists of the oocyte and the follicular envelope, which is composed of
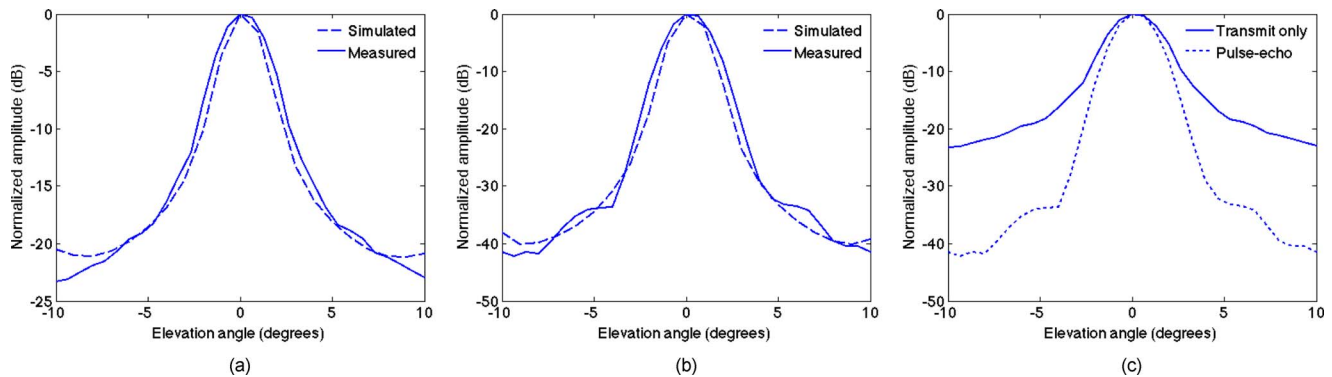
Fig. 5 Measured and simulated elevation beam profiles of a 20-deg sector scan: (a) transmit only, (b) pulse-echo, and (c) transmit only versus pulse-echo.
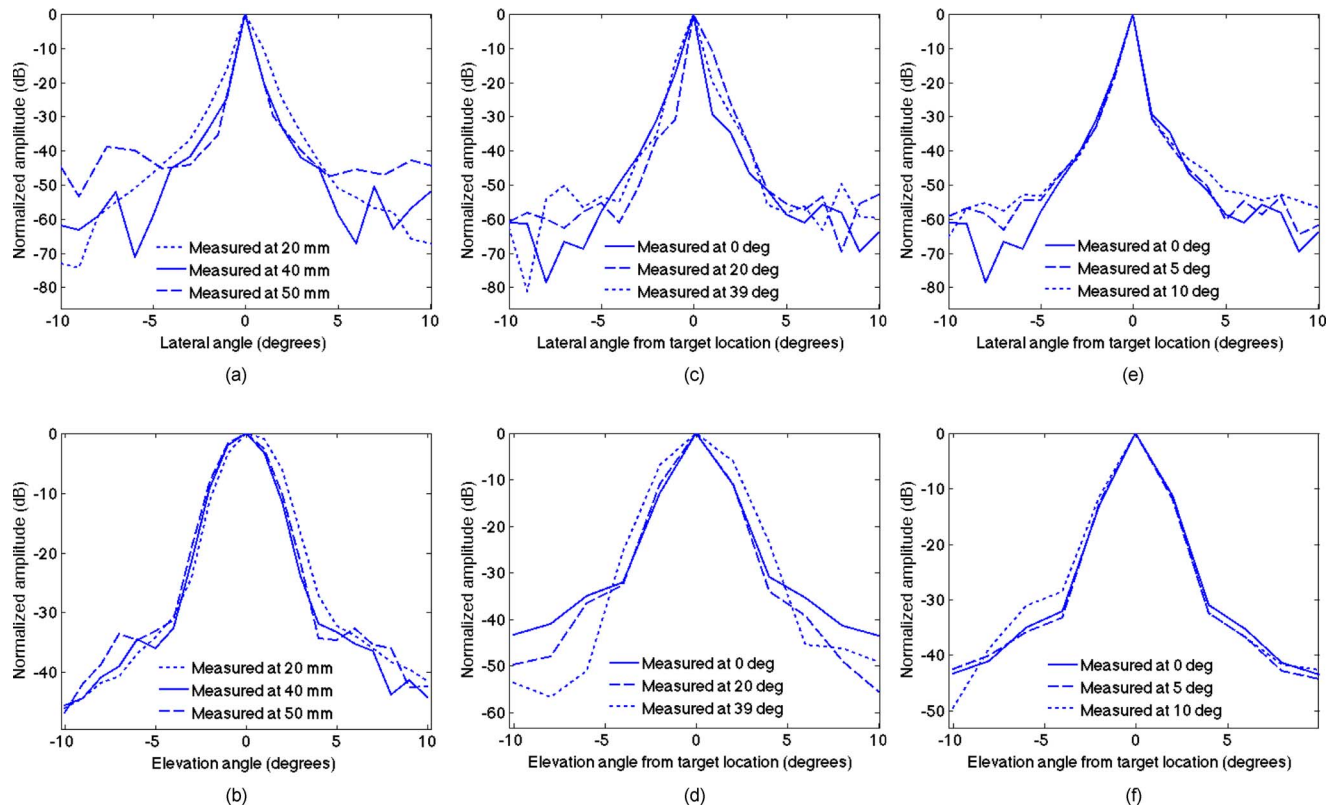
Fig. 6 Two-way beam profile measurements using a music-wire target. First group of measurements at various axial depths: (a) azimuth beam profile and (b) elevation beam profile. Second group of measurements at various angular positions in the azimuth-axial plane: (c) azimuth beam profile and (d) elevation beam profile. Third group of measurements at various angular positions in the elevation-axial plane: (e) azimuth beam profile and (f) elevation beam profile.

granulosa cells and an outer membrane. Follicles migrate from the innermost part of the cortex to the surface as they mature to become antral follicles, which increase fluid accumulation in their antrum.[47] Antral follicles are easily imaged with ultrasound and appear hypoechoic. As the follicles are located in the cortex of the ovary, which is comprised mostly of dense cellular connective tissue with hyperechoic appearance on ultrasound, excellent contrast with ultrasound imaging is generally achieved between the follicular fluid and the cortex. Figures 8(a), 8(c), and 8(e) show a series of pulse-echo ultrasound images of the first excised ovary of a young, but sexually mature pig. These images correspond to different elevation planes obtained by changing the electronic focus in steps of 0.7 deg. One can distinguish many antral follicles across the whole ovary. Figs. 8(b), 8(d), and 8(f) show the coregistered photoacoustic images superimposed on top of the pulse-echo images. Optical absorption occurs in the central area of the ovary along the long axis, but no absorption is observed around the follicles or the cortex of the ovary itself. The highly absorptive area corresponds to the medulla, where blood vessels, lymphatic vessels, and nerves run from the mesovarium, which attaches the ovary to the uterus via the broad ligament.[48] Excellent agreement between the coregistered images and HE staining of a corresponding histological section of the ovary is apparent when comparing the previous images to Fig. 8(g).

Antral follicles vary in size; they grow from less than a millimeter to a few centimeters. This is more evident in the preovulation stage, where many changes take place in the preovulatory follicle. Shortly before follicular rupture, expansion of the follicle occurs with marked hyperaemia in the theca of the preovulatory follicle due to increased vascularity and increased permeability of its capillaries.[47] These changes can be observed in the coregistered ultrasound and photoacoustic image of the second ovary, as shown in Fig. 9. A 1 cm in diameter antral follicle can be observed in the ultrasound image, while optical absorption due to the increase of blood in the theca stands out around the follicle in the photoacoustic image. This corresponds well to histology as indicated by the smaller arrow in Fig. 9(c).

In primates and pigs, the antrum of the follicle fills with blood and lymph after ovulation, and vessels from the theca grow into the antrum and branch to form a network of capillaries and fibroblasts that develop into the corpus luteum.[47] This process can be seen in the corpus luteum shown in Fig. 9(c) larger arrow), which is partially filled with blood and connective tissue. Poor contrast is observed with pulse-echo ultrasound, but good contrast is achieved with photoacoustic imaging due to optical absorption in the surrounding theca and the blood-filled antrum.

Figure 10 shows the results from our third imaged ovary. In the ultrasound image, the only features that stand out are two antral follicles that are just under 5 mm in diameter [smaller arrows in figure 10(c)]. However, photoacoustic imaging reveals the presence of a highly absorptive area, which represents a hemorrhagic corpus luteum [larger arrow in fig-
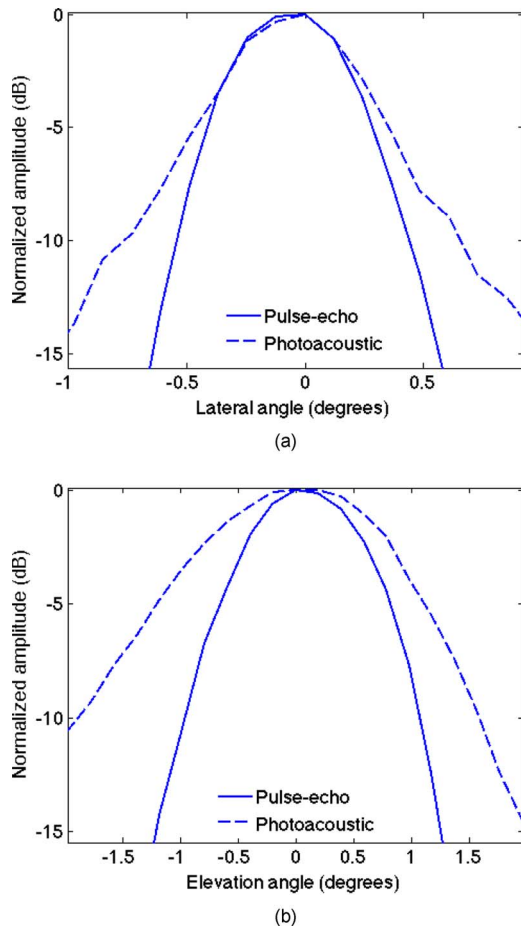
Fig. 7 Resolution measurement in pulse-echo and photoacoustic modes performed at the elevation focus: (a) azimuth resolution and (b) elevation resolution.
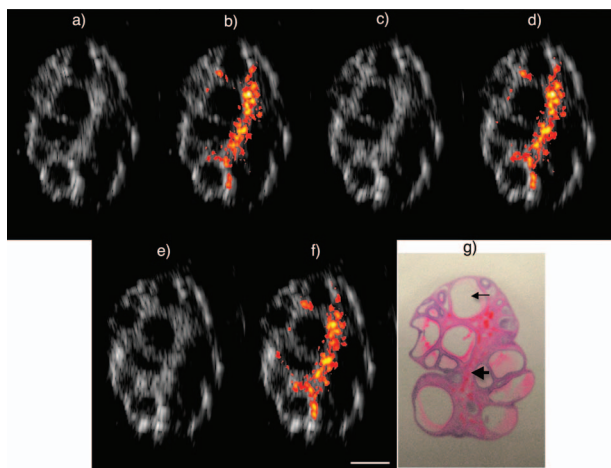
Fig. 8 Coregistered images of ovary 1 at different elevation planes. (a), (c), and (d) show ultrasound-only images. (b), (d), and (f) show photoacoustic images on top of the ultrasound images. Each pair of ultrasound and coregistered images was obtained by changing the electronic focus in elevation in steps of 0.7 deg. (g) HE stained histo-logical slide. The white bar represents 5 mm.
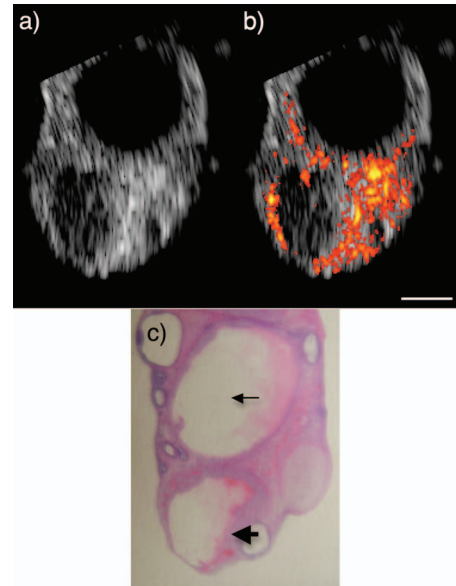
Fig. 9 Coregistered images of ovary 2. (a) Ultrasound-only image. (b) Photoacoustic image on top of the ultrasound image. (c) HE stained histological slide. The white bar represents 5 mm.

ure 10(c)]. In addition, photoacoustic imaging shows absorption around the antral follicles due to the vascularity in the theca of the follicles. HE staining of the corresponding histological slide shows excellent agreement with the follicles seen by ultrasound and the corpus luteum seen by photoacoustic imaging.

4 Discussion

We demonstrate the excellent 3-D imaging capability of our 1.75-D ultrasound array system. The system data acquisition speed is currently slow and only suitable for *ex vivo* studies. *Ex vivo* studies of normal and malignant ovarian tissue are important steps toward understanding the vascular contrast of such a complex organ in the normal and diseased conditions.

Imaging results of the ovaries have shown excellent correlation between highly vascularized ovarian tissue structures, such as the corpus luteum, seen by photoacoustic imaging and histology. Results have also shown excellent coregistration
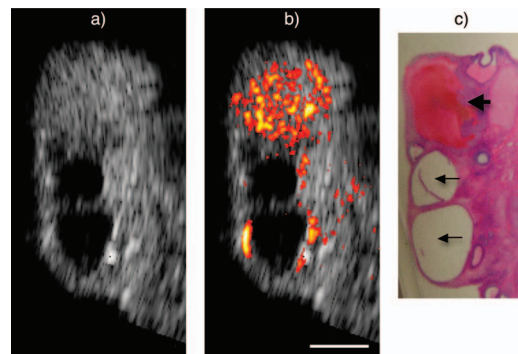
Fig. 10 Co-registered image of ovary 3. (a) Ultrasound-only image. (b) Photoacoustic image on top of the ultrasound image. (c) HE stained histological slide. The white bar represents 5 mm.

between photoacoustic imaging and pulse-echo ultrasound. It is interesting to observe that the highly vascularized corpus luteum is not quite visible in the ultrasound image, but stands out in the photoacoustic image due to its vascularity, which suggests that photoacoustic imaging may have a significant advantage over traditional ultrasound in differentiating early cancer from corpus luteal cysts and endometriomas, currently conditions difficult to differentiate clinically and ultrasonographically. The limited ability of ultrasound to differentiate these benign conditions from early cancers leads to missed cancers when there is reluctance to subject a woman to surgery without more evidence of cancer, and to increased morbidity from potentially unnecessary surgery when the surgeon is aggressive in trying to prevent cancer. Early stage ovarian cancers with neovascularization due to tumor angiogenesis are not detectable by ultrasound, but we expect, based on this early data, that they will be detected by photoacoustic technique. Our hypothesis has to be validated by future *ex vivo* and *in vivo* studies.

The current study was performed in a controlled environment, which permits optimal delivery of light to the ovary for proper signal generation. Additionally, any background photoacoustic signals generated from the surrounding tissue that could interfere with the signals from an imaged ovary were absent. These favorable conditions are necessary for an accurate initial assessment of the optical properties of the ovary. However, challenges arise in an *in vivo* imaging condition, where the light delivery needs to be optimized and the interference from the surrounding tissue needs to be minimized.

In conventional ultrasound, ovaries can be imaged noninvasively through the vagina. The vaginal wall is typically less than 1 cm thick, and in the anteverted uterus, the ovaries are positioned typically at about the cervix level and are easily accessed with a transvaginal ultrasound probe. The ultrasound attenuation is significantly reduced in a transvaginal approach, relative to the abdominal approach in which the ultrasound encounters about 3 to 5 cm of abdominal wall thickness (depending on the size of the patient). A similar approach for photoacoustic imaging would be necessary to maximize light delivery to the ovary and to minimize photoacoustic signal attenuation from the imaged ovary to the ultrasound transducer. This requires a backward-mode imaging configuration, where illumination and detection are performed from the same location. Optical fibers can be distributed around the transvaginal ultrasound probe for delivering the light, and the transvaginal ultrasound probe can be used for both pulse-echo and photoacoustic imaging.

The reported photoacoustic images of normal porcine ovaries were normalized to the maximum value for each ovary, and they show qualitative distribution of the optical absorption. Based on our initial experience with pig and human ovarian samples, we have found that this normalization approach can identify local abnormal areas with high blood content compared with the surrounding tissue. Due to strong dependence on feature geometry, orientation, size, as well as density and collagen content, reconstruction with a photoacoustic technique of quantitative optical absorption changes of ovary remains a technical challenge and will be pursued in future studies.

5   Summary

We characterize a 1.75-D ultrasound array system developed in our laboratory, which provides coregistered ultrasound and photoacoustic images for 3-D visualization of ovarian tissues. Using the aforementioned system, we focus on understanding and characterizing the photoacoustic properties of normal ovarian tissue from pigs, and correlating these images with well-established pulse-echo ultrasound and histological sections. Our initial results show excellent correlation between highly vascularized ovarian tissue structures, such as the corpus luteum, seen by photoacoustic imaging and histology. Results also show excellent coregistration between photoacoustic imaging and pulse-echo ultrasound.

Our next step is to develop a coregistered ultrasound and photoacoustic transvaginal probe for real-time noninvasive evaluation of ovaries. The long-term goal is the detection of angiogenic changes in the ovary and correlating these changes with early cancer. The ability to detect these changes in the ovary with a noninvasive and real-time imaging modality would greatly enhance the care for women at risk for ovarian cancer.

References

1. V. G. Andreev, A. A. Karabutov, S. V. Solomatin, E. V. Savateeva, V. Aleinikov, Y. V. Zhulina, R. D. Fleming, and A. Oraevsky, "Optoacoustic tomography of breast cancer with arc-array transducer," in *Biomedical Optoacoustics*, *Proc. SPIE* **3916**, 36–47 (2000).
2. R. A. Kruger, P. Liu, Y. R. Fang, and C. R. Appledorn, "Photoacoustic ultrasound (PAUS)—reconstruction tomography," *Med. Phys.* **22**(10), 1605–1609 (1995).
3. A. Oraevsky and A. A. Karabutov, "Ultimate sensitivity of time-resolved optoacoustic detection," in *Biomedical Optoacoustics*, *Proc. SPIE* **3916**(1), 228–239 (2000).
4. X. Wang, Y. Pang, G. Ku, X. Xie, G. Stoica, and L. V. Wang, "Noninvasive laser-induced photoacoustic tomography for structural and functional *in vivo* imaging of the brain," *Nat. Biotechnol.* **21**(7), 803–806 (2003).
5. B. T. Cox and P. C. Beard, "Fast calculation of pulsed photoacoustic fields in fluids using k-space methods," *J. Acoust. Soc. Am.* **117**(6), 3616–3627 (2005).
6. C. G. Hoelen, F. F. de Mul, R. Pongers, and A. Dekker, "Three-dimensional photoacoustic imaging of blood vessels in tissue," *Opt. Lett.* **23**(8), 648–650 (1998).
7. A. Karabutov, E. V. Savateeva, N. B. Podymova, and A. A. Oraevsky, "Backward mode detection of laser-induced wide-band ultrasonic transients with optoacoustic transducer," *J. Appl. Phys.* **87**, 2003–2014 (2000).
8. R. A. Kruger, D. R. Reinecke, and G. A. Kruger, "Thermoacoustic computed tomography—technical considerations," *Med. Phys.* **26**(9), 1832–1837 (1999).
9. G. Ku, X. Wang, G. Stoica, and L. V. Wang, "Multiple-bandwidth photoacoustic tomography," *Phys. Med. Biol.* **49**(7), 1329–1338 (2004).
10. G. Paltauf, J. A. Viator, S. A. Prahl, and S. L. Jacques, "Iterative reconstruction algorithm for optoacoustic imaging," *J. Acoust. Soc. Am.* **112**(4), 1536–1544 (2002).
11. S. Sethuraman, J. H. Amirian, S. H. Litovsky, R. W. Smalling, and S. Y. Emelianov, "Spectroscopic intravascular photoacoustic imaging to differentiate atherosclerotic plaques," *Opt. Express* **16**(5), 3362–3367 (2008).

12. L. V. Wang and H. Wu, *Biomedical Optics: Principles and Imaging*, Wiley, Hoboken, NJ (2007).
13. L. V. Wang, "Tutorial on photoacoustic microscopy and computed tomography," *IEEE J. Sel. Top. Quantum Electron.* **14**(1), 171–179 (2008).
14. L. V. Wang, "Prospects of photoacoustic tomography," *Med. Phys.* **35**(12), 5758–5767 (2008).
15. Y. Xu and L. V. Wang, "Time reversal and its application to tomography with diffracting sources," *Phys. Rev. Lett.* **92**(3), 033902 (2004).
16. J. J. Niederhauser, M. Jaeger, R. Lemor, and P. Weber, "Combined ultrasound and optoacoustic system for real-time high-contrast vascular imaging *in vivo*," *IEEE Trans. Med. Imaging* **24**(4), 436–440 (2005).
17. P. Vaupel, F. Kallinowski, and P. Okunieff, "Blood flow, oxygen and nutrient supply, and metabolic microenvironment of human tumors: a review," *Cancer Res.* **49**(23), 6449–6465 (1989).
18. N. Weidner, J. P. Semple, W. R. Welch, and J. Folkman, "Tumor angiogenesis and metastasis—correlation in invasive breast carcinoma," *N. Engl. J. Med.* **324**(1), 1–8 (1991).
19. J. Gamelin, A. Aguirre, A. Maurudis, F. Huang, D. Castillo, L. V. Wang, and Q. Zhu, "Curved array photoacoustic tomographic system for small animal imaging," *J. Biomed. Opt.* **13**(2), 024007 (2008).
20. M. Xu and L. V. Wang, "Photoacoustic imaging in biomedicine," *Rev. Sci. Instrum.* **77**(4), 041101 (2006).
21. R. A. Kruger, W. L. Kiser, D. R. Reinecke, G. A. Kruger, and K. D. Miller, "Thermoacoustic molecular imaging of small animals," *Mol. Imaging* **2**(2), 113–123 (2003).
22. K. Mehta, R. Lacewell, P. M. Henrichs, and A. A. Oraevsky, "128-channel laser optoacoustic imaging system (LOIS-128) for breast cancer diagnostics," *Proc. SPIE* **6086**, 608609 (2006).
23. V. Kozhushko, T. Khokhlova, A. Zharinov, and I. Pelivanov, "Focused array transducer for two-dimensional optoacoustic tomography," *J. Acoust. Soc. Am.* **116**(3), 1498–1506 (2004).
24. R. A. Kruger, W. L. Kiser, D. R. Reinecke, and G. A. Kruger, "Thermoacoustic computed tomography using a conventional linear transducer array," *Med. Phys.* **30**(5), 856–860 (2003).
25. B. Yin, D. Xing, Y. Wang, Y. Zeng, Y. Tan, and Q. Chen, "Fast photoacoustic imaging system based on 320-element linear transducer array," *Phys. Med. Biol.* **49**, 1339–1346 (2004).
26. R. Zemp, R. Bitton, M. Li, K. Shung, G. Stoica, and L. V. Wang, "Photoacoustic imaging of the microvasculature with a high-frequency ultrasound array transducer," *J. Biomed. Opt.* **12**(1), 010501 (2007).
27. S. Park, S. Mallidi, A. B. Karpiouk, and S. Aglyamov, "Photoacoustic imaging using array transducer," *Proc. SPIE* **6437**, 643714 (2007).
28. C. G. Hoelen and F. F. de Mul, "Image reconstruction for photoacoustic scanning of tissue structures," *Appl. Opt.* **39**(31), 5872–5883 (2000).
29. K. P. Köstli and P. C. Beard, "Two-dimensional photoacoustic imaging by use of Fourier-transform image reconstruction and a detector with an anisotropic response," *Appl. Opt.* **42**(10), 1899–1908 (2003).
30. M. Xu and L. V. Wang, "Universal back-projection algorithm for photoacoustic computed tomography," *Phys. Rev. E* **71**(1 Pt 2), 016706 (2005).
31. J. F. Gelly and J. M. Bureau, "Two-dimensional (2D) transducer arrays for medical ultrasonic imaging," *RBM-Revue Europeenne de Technologie Biomedicale* **20**, 243–246 (1998).
32. A. T. Fernandez, K. Gammelmark, J. J. Dahl, and C. G. Keen, "Synthetic receive beamforming and image acquisition capabilities using an 8×128 1.75 D array," *IEEE Trans. Ultrason. Eng.* **50**(1), 40–57 (2003).
33. K. Y. Saleh and N. B. Smith, "A 63 element 1.75 dimensional ultrasound phased array for the treatment of benign prostatic hyperplasia," *Biomed. Eng. Online* **4**(39), 1–14 (2005).
34. W. J. Hoskins, "Prospective on ovarian cancer: why prevent?" *J. Cell Biochem. Suppl.* **23**, 189–199 (1995).
35. American Cancer Society, *Cancer Facts & Figures 2008*, American Cancer Society, Atlanta, GA (2008).
36. "Ovarian cancer: screening, treatment, and followup," *NIH Consens Statement* **12**(3), 1–30 (1994).
37. J. Tammela and S. Lele, "New modalities in detection of recurrent ovarian cancer," *Curr. Opin. Obstet. Gynecol.* **16**(1), 5–9 (2004).
38. A. Shaaban and M. Rezvani, "Ovarian cancer: detection and radiologic staging," *Clin. Obstet. Gynecol.* **52**(1), 73–93 (2009).
39. P. Guo, S. Yan, and Q. Zhu, "Elevation beamforming performance of a 1.75 D array," *Proc.-IEEE Ultrason. Symp.* **2**, 1113–1116 (2001).
40. S. Yan, "A DSP-based real-time optical Doppler tomography system—beamforming study of a 10×128 1.75D ultrasound array," PhD thesis, Dept. of Electrical and Computer Engineering, Univ. of Connecticut (2005).
41. P. Guo, "Three-dimensional ultrasound imaging and its applications in combined near-infrared optical imaging and co-registered photoacoustic imaging," PhD thesis, Dept. of Electrical and Computer Engineering, Univ. of Connecticut (2007).
42. G. W. C. Kaye, T. H. Laby, and J. G. Noyes, *Tables of Physical and Chemical Constants*, Longman, London (1995).
43. J. L. Schwartz and B. D. Steinberg, "Ultrasparse, ultrawideband arrays," *IEEE Trans. Ultrason. Ferroelectr. Freq. Control* **45**(2), 376–393 (1998).
44. J. A. Jensen and N. B. Svendsen, "Calculation of pressure fields from arbitrarily shaped, apodized, and excited ultrasound transducers," *Ultrasonics* **39**(2), 262–267 (1992).
45. J. A. Jensen, "FIELD: a program for simulating ultrasound systems," *Med. Biol. Eng. Comput.* **34**(1), 351–353 (1996).
46. B. D. Steinberg, *Principles of Aperture and Array System Design: Including Random and Adaptive Arrays*, Wiley-Interscience, New York (1976).
47. H. Peters and K. P. McNatty, *The Ovary: A Correlation of Structure and Function in Mammals*, University of California Press, Los Angeles (1980).
48. T. D. S. Rod R. Seeley, and P. Tate, *Anatomy and physiology*, McGraw-Hill, New York (2003).